Journal of Hydrology 612 (2022) 128182

Contents lists available at ScienceDirect

Journal of Hydrology

journal homepage: www.elsevier.com/locate/jhydrol

Research papers

Analysis of two sources of variability of basin outflow hydrographs computed with the 2D shallow water model Iber: Digital Terrain Model and unstructured mesh size

Gonzalo García-Alén [a,*], Jose González-Cao [b], Diego Fernández-Nóvoa [b], Moncho Gómez-Gesteira [b], Luis Cea [a], Jerónimo Puertas [a]

[a] Universidade da Coruña, Water and Environmental Engineering Group, Department of Civil Engineering, School of Civil Engineering, Elviña, 15071 A Coruña, Spain
[b] Environmental Physics Laboratory, CIM-UVIGO, Universidade de Vigo, Campus As Lagoas, 32004 Ourense, Spain

ARTICLE INFO

This manuscript was handled by Andras Bardossy, Editor-in-Chief, with the assistance of Szilágyi József, Associate Editor

Keywords:
SRTM
IGN
Digital elevation model
Iber
Mesh size
Runoff

ABSTRACT

Modelling hydrological processes with fully distributed models based on the shallow water equations implies a high computational cost, which often limits the resolution of the computational mesh. Therefore, in practice, modellers need to find a compromise between spatial resolution, numerical accuracy and computational cost. Moreover, this balance is probably related to the accuracy and resolution of the underlying Digital Terrain Model (DTM). In this work, it is studied the effect of the DTM resolution and the size of the computational mesh on the results and on the runtime of a hydrological model based on the 2D shallow water equations. Seven rainfall events in four different basins have been modelled using 3 DTMs and 3 different mesh resolutions. The results obtained highlight the relevance of the vertical accuracy versus the horizontal resolution of the DTMs. Furthermore, it has been observed that mesh resolutions greater than 25 m, together with LiDAR-based DTMs with horizontal resolution greater than 25 m, provide comparable outflow hydrographs.

1. Introduction

Hydrological models are commonly used to reproduce and understand the water fluxes that compose the hydrological cycle of a basin (Refsgaard and Storm, 1990; Schaake et al., 1996). The birth of this type of models took place in the 1960s and since then there have been a large number of improvements both in the development of new numerical methods and in the physical representation of the numerical model (Perumal and Price, 2017; Pham and Tsai, 2017; Singh, 2018). Among the most important advances, one can highlight the flourishing of remote sensing systems, particularly satellites and radars, together with the progress of Geographic Information Systems (GIS). The combination of the two has made it possible to work with spatial data on climate, morphology, geology, land use or, inter alia, topography (Muhadi et al., 2020; Mujumdar and Nagesh Kumar, 2012). The development of GIS has, in turn, driven the growth of databases incorporating high spatial resolution information (Berhanu et al., 2013; Lehner and Döll, 2004; Tsangaratos et al., 2017; Uuemaa et al., 2020). This, coupled with the recent advances in high performance computing, has led to the fact that spatially distributed models are gaining momentum against lumped and semi-distributed models (Chen et al., 2017; Fraga et al., 2019; Kang and Sridhar, 2017; Laiolo et al., 2016).

One of the basic input data whose use is ubiquitous in all hydrological models are Digital Terrain Models (DTM). DTMs represent the continuously varying topographic surface of the Earth and provide hydraulic modelers with an efficient tool to extract the hydrological characteristics of a watershed (terrain slope, drainage networks, etc.). Nevertheless, its applicability in distributed models raises a question that was already stated by Quinn et al. (1991) but which is still a matter of research (Bomers et al., 2019; Caviedes-Voullième et al., 2012; Costabile and Costanzo, 2021; Fernández-Pato et al., 2016; Hou et al., 2018a) namely, what DTM resolution is needed to achieve a correct representation of the relevant hydrological processes? This question goes hand in hand with the following: what is the most appropriate mesh size for a given DTM resolution? These questions become even more complex if we consider studies such as Marsh et al. (2018) where it is indicated that the mesh configuration is not only constrained by topography, but must also correctly represent surface and sub-surface

* Corresponding author.
E-mail address: g.glores@udc.es (G. García-Alén).

https://doi.org/10.1016/j.jhydrol.2022.128182
Received 8 April 2022; Received in revised form 6 June 2022; Accepted 4 July 2022
Available online 11 July 2022

features, along with landscape variability. Moreover, the DTM resolution should be related to the spatial scale of the hydrological processes that we want to represent. On the other hand, for a proper exploitation of the DTM resolution, the cell size of the computational mesh should be equal to, or smaller than, the DTM cell size. However, in large scale fully distributed models the computational cost of a very fine mesh may be unaffordable. Moreover, in addition to the spatial resolution of the DTM and the mesh, the vertical accuracy of the DTM is also relevant, since it can lead to significant inaccuracies in model predictions. Undoubtedly, the accuracy and resolution of DTMs must be taken into account in the calculation processes, and authors such as Habtezion et al. (2016) have long since reflected on whether hydrological modelers are fully aware of the limitations of DTMs.

There are many studies that have explored the impact of the DTM quality in different kinds of hydrological models. Vaze et al. (2010) studied the impact of DTM accuracy and resolution on topographic indices using as a case study a 32.000 ha catchment located in Australia. It was concluded that the quality of DTM-derived hydrological features is very sensitive to DTM accuracy and resolution. Their results suggest that the DTM with the highest resolution available should be used and, in those cases where computational time constraints do not allow its use, a resampling to a lower resolution should be done instead of directly taking a DTM with a lower resolution. Other authors, such as Mukherjee et al. (2012) or Courty et al. (2019), directly analysed the accuracy of different freely available DTMs, helping to better understand the limitation of such products (Zhao et al., 2021). In contrast, several authors have focused on analysing the role of the grid size in hydromorphological studies (Dietrich et al., 1995; Gómez Gutiérrez et al., 2015; Kienzle, 2004; Wilson et al., 2000). In order to compute topographic characteristics, Claessens et al. (2005) looked at the impact of using different grid sizes (10, 25, 50 and 100 m), while Paulin et al. (2010) investigated how different grid sizes (1, 5, 10 and 30 m) affected the cartographic depiction of small and deep landslides. However, works such as Tarolli and Tarboton (2006), where the relation between mesh sizes and DTM resolution is studied, are less common.

The application of hydrological models based on the 2D shallow water equations is becoming a common approach in rainfall-runoff simulations at the catchment scale (Bellos et al., 2020; Caviedes-Voullième et al., 2012; Cea and Bladé, 2015; Costabile et al., 2012; Fernández-Pato et al., 2018; Hou et al., 2018b; Liang et al., 2015; Ni et al., 2020; Simons et al., 2014; Uber et al., 2021). One of the most valued features of such complex models is the fact that they allow hydrodynamic calculations to be carried out on a basin scale, but taking into account local flow phenomena. In order to capture the potential effects that hydraulic structures, such as bridges or weirs, have on the propagation of the flood, it is required a high resolution numerical model (e.g., Macchione and Lombardo, 2021). Although at the local scale the hydrostatic pressure approximation (essential assumption in 2D-SWE models) is not valid in the surroundings of these structures, these models still provide reliable results at the catchment scale (García-Alén et al., 2021; Luis et al., 2022). In the definition of the computational mesh of the model, despite recent advances in High Performance Computing (HPC) (García-Feal et al., 2018; Lacasta et al., 2015; Petaccia et al., 2016; Sanders and Schubert, 2019; Vacondio et al., 2014; Xia et al., 2019), modellers often have to make a balance between a fine mesh that correctly reproduces the topography of the terrain (Costabile and Macchione, 2015) and a feasible computational cost. Some authors have analysed the optimisation of the computational domain by exploring the advantages of mixed-mesh (Bomers et al., 2019; Hoch et al., 2018) and adaptive grids (Hu et al., 2019; Savant et al., 2019). Other authors have explored the mesh refinement by the detection of key topographic features (Costabile and Costanzo, 2021; Ferraro et al., 2020; Hou et al., 2018a).

In this paper we study the interactions between the DTM and computational mesh resolutions on rainfall-runoff simulation with a fully distributed hydrodynamic model based on the 2D-SWE. This analysis is carried out by studying the degeneracy of the output hydrograph observed with several DTMs and mesh resolutions, together with the analysis of the different runtimes. The output hydrograph obtained with the best-resolution mesh and DTM was used as reference result (synthetic true). The results obtained in 7 rainfall events occurring in 4 hydrological basins are studied. For each rainfall event, 9 model configurations were run by combining 3 freely distributed DTMs with 3 different mesh sizes. Regarding the DTMs, the horizontal resolutions used were 5, 25 and 30 m. The 5 and 25 m DTMs are LiDAR-based products offered by the Spanish National Geographic Institute (IGN) and, therefore, only available for Spain; while the 30 m DTM is product provided by the Shuttle Radar Topography Mission (SRTM) and global coverage. As for the computational meshes used, 3 different resolutions have been defined for each basin and their element size has been adapted to the size of each basin, always maintaining a ratio between element sizes of 1, 2.5 and 10.

2. Case studies and available data

2.1. Description of the watersheds

Four river basins located in Spain were selected to undertake this study: Izas, Caldo, Landro and Genil river basins (Fig. 1). In the choice of the study cases, priority has been given to the selection of basins of different size (from 0.33 to 3750 km^2), mean slope (from 7° to 20°) and precipitation regime (their maximum daily precipitation varies from 36 to 142.8 mm). A summary of the main characteristics of each watershed is included in Table 1. The Genil river basin represents a large low sloped watershed marked by a Mediterranean climate with a low base flow during most of the year but with intense rainfall events that produce strong peak flows. On the other hand, the Caldo and Landro basins have a steeper topography and are located in an Atlantic climate region characterized by a more uniform rainfall regime. Finally, the Izas basin is a small mountain catchment located in the Pyrenees, with steep slopes and a very low concentration time.

The Izas Catchment is located in the Central Spain Pyrenees, in the Upper Gállego Valley, near the Spain-France border. The catchment occupies an extension of 0.33 km^2 and is located at an altitude of over 2000 m.a.s.l. The catchment is predominantly east orientated, with some areas also facing north or south. The main ravine is a tributary of the Escarra river which, in turn, is a tributary of the Gállego river which, finally, debouches into the Ebro river. The entire catchment is located above the upper forest limit and exemplifies the general conditions of subalpine areas of the Pyrenees. Subalpine and alpine grassland domain the landscape, although some rocky outcrops are also present in the upper and steeper slopes (Lana-Renault et al., 2014; López-Moreno et al., 2013; Revuelto et al., 2017). Rainy season in this basin is between October and May (Alvera and García-Ruiz, 2000). The Caldo river catchment, with an area of 38 km^2, is located in north-west Spain in the border with Portugal. Land coverage is dominated by grasslands, coniferous and leaf forest and different kind of crops (Meléndez-Asensio and del Pozo-Tejado, 2019). The region is located in the transition between the Mediterranean and Eurosiberian biogeographic zones, therefore, the climate is temperate oceanic sub-Mediterranean (Ninyerola et al., 2005). The Landro river is located in north-western Spain. The total area of its basin is 199 km^2 and its mean altitude is below 1000 m.a.s.l. This river is born in the Gistral mountain range and flows into the Cantabrian Sea in the Viveiro estuary. The watershed is covered by eucalyptus and pine forests and scrublands with only a small proportion of cultivated areas in the river floodplains. The soil permeability of the basin is low (Barja and Lestegas, 1992). Rainfall is quite regular throughout the year, which reflects an oceanic rainfall regime, with maximum flows in winter and minimum flows in summer. The Genil river basin is located in southern Spain and its catchment covers an area of 8200 km^2. In its central area is located the Iznájar reservoir (981 hm^3), which is one of the largest reservoirs in Spain. This reservoir was

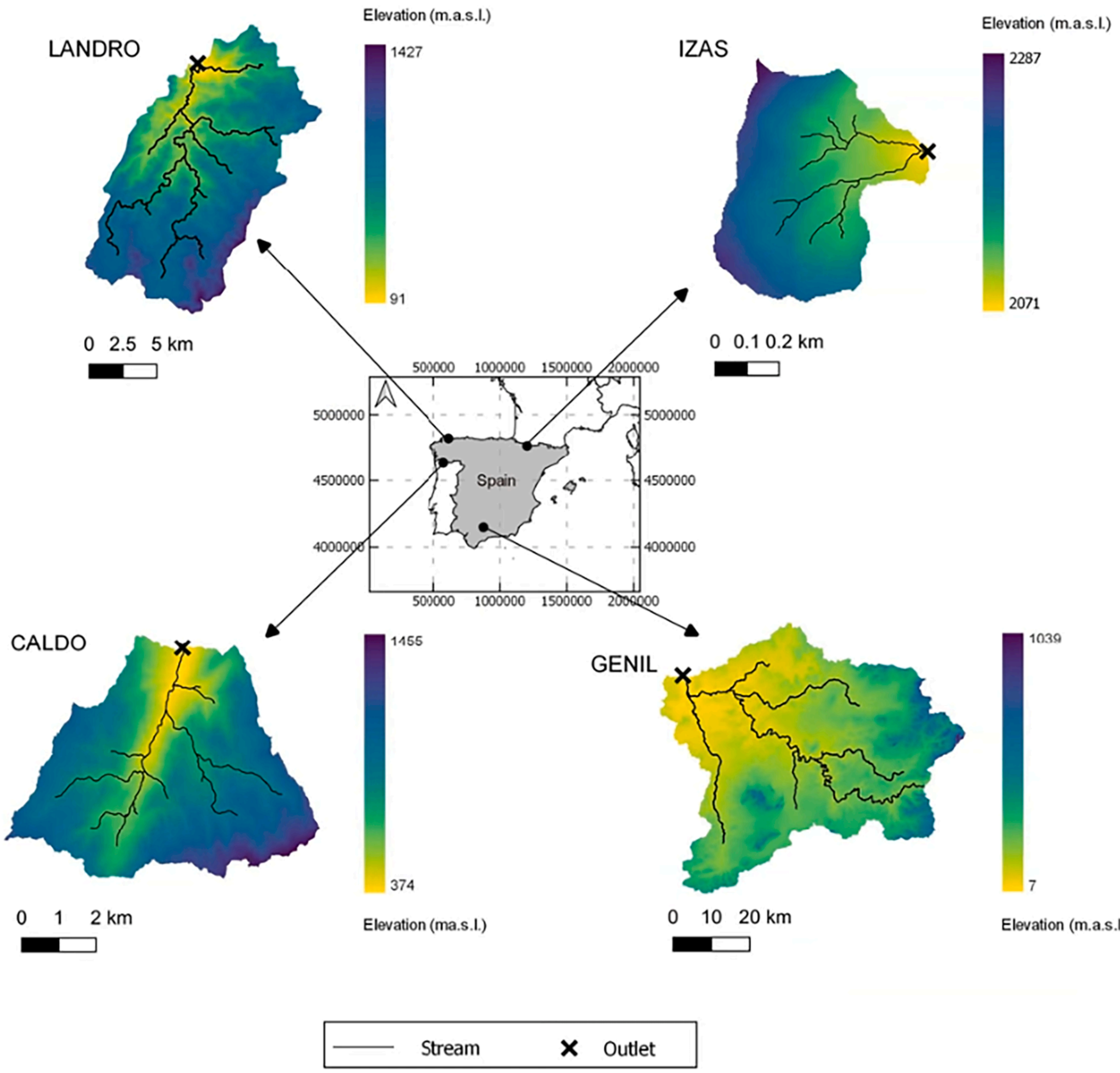

Fig. 1. Study catchments.

Table 1
Main characteristics of the study basins.

Watershed	Location	Area (km^2)	Mean slope (°)	Altitude range (m.a.s.l.)	Average annual precipitation (mm)	Average annual maximum daily precipitation (mm)
Izas	North-Eastern Spain	0.33	16	2060-2280	2000	36
Caldo	North- western Spain	38	20	370-1200	1800	41
Landro	North- western Spain	199	15	0-1033	1412	61.8
Genil	Southern Spain	3750	7	90-1438	500	142.8

designed to absorb the ordinary floods of the river and it completely controls the downstream discharge. Thus, it divides the Genil river basin into two subbasins: Upper and Lower Genil. Only the Lower Genil subbasin has been analysed in this study. This basin begins at the Iznájar reservoir and ends in the municipality of Écija. The study area has a total surface of 3750 km^2. It is a typical Mediterranean landscape, with fragile natural ecosystems and insufficient rainfall to allow for quick vegetation regeneration and long-term human use. The climate is arid, with an annual rainfall of 500 mm. There is a wide range of vegetation cover, including annual crops, grassland, bushes and woodland. However, given that the main economic activity in the area is agriculture, irrigated crops and rainfed olive groves account for a significant area of the basin.

2.2. Rainfall events

Seven rainfall events have been modelled in the study basins (1 event in the Izas basin and 2 events in the Caldo, Landro and Genil basins). All of these are isolated rainfall events that produced high peak flows in the river. The observed precipitation and flow data were obtained from different sources for each catchment. In the Izas basin data were provided by the Pyrenean Institute of Ecology (IPE). In the Caldo basin, data were provided by the Miño-Sil River Basin Management Authority (CHMS). In the Landro basin data were provided by the Galician Meteorological Agency (Meteogalicia). Finally, in the Genil basin data were provided by the Guadalquivir River Basin Management Authority

(CHG). Main characteristics of the rainfall events, along with the peak discharge and volume of the observed hydrograph, are listed in Table 2.

Due to the small size of the Izas and Caldo catchments, a spatially homogeneous rainfall was assumed in these two basins. In the case of the Landro and Genil basins, the spatial distribution of rainfall was estimated from rain gauge and radar data.

3. Methodology

3.1. Digital terrain models

The three DTMs used in this study are the following: (1) the DTM provided by the Spanish National Geographic Institute (IGN) at a 5 m resolution (IGN-CNIG, 2021); (2) the DTM provided by the Spanish IGN at a 25 m resolution; and (3) the Shuttle Radar Topography Mission (SRTM) DTM with a grid size of 1 arc-second (approximately 30 m) (Farr et al., 2007; Werner, 2001). The different spatial resolutions of the 3 DTMs are visually compared in Fig. 2. Hereafter, these DTMs will be referred to as DMT05, DTM25 and DTM30, respectively.

The first two DTMs are derived from the Spanish Aerial Orthophotography National Plan in Spain (PNOA), and are freely distributed by the Spanish National Geographic Institute (IGN) (IGN-CNIG, 2021). DTM05 was obtained by automatic correlation and interactive stereoscopic debugging for the PNOA initiative. Its RMSE in the vertical direction is estimated to be lower than 50 cm (PNOA, 2015). DTM25 was generated by interpolation of the DTM05, maintaining a RMSE value for the elevation differences of 2.9 m (Martínez et al., 2004).

NASA Shuttle Radar Topography Mission (SRTM) datasets were obtained from a collaborative effort by the National Aeronautics and Space Administration (NASA) and the National Geospatial-Intelligence Agency (NGA), as well as the participation of the German and Italian space agencies, with the purpose of generating a near-global DTM of the Earth using radar interferometry. The DTM30 ("SRTM V3.0, 1arcsec") (Farr et al., 2007) is a near-global DTM with a 1 arc second (≈30 m) resolution comprising a combination of data from the SRTM and the U. S. Geological Survey's GTOPO30 data set. The primary goal of creating the Version 3 data was to eliminate voids that were present in earlier versions of SRTM data. The global and free availability (NASA JPL, 2013) of the SRTM DTMs has led to its application in multiple hydrological studies (Alsdorf et al., 2007; Hancock et al., 2006; Sreedevi et al., 2009). According to its mission objectives, SRTM DTMs are expected to have a vertical RMSE of 10 m (Chen et al., 2020; Farr et al., 2007; Kellndorfer et al., 2004; Mukul et al., 2015), even though validation studies reported a vertical RMSE in Europe of 3.8 m (Carrera-Hernandez, 2021; Mukul et al., 2017; Santillan and Makinano-Santillan, 2016; Szabó et al., 2015).

Table 2
Main characteristics of the selected events and their corresponding hydrograph.

Event number	Watershed	Duration (h)	Starting date	Total rainfall depth (mm)	Q_{peak} (m^3/s)	Runoff depth (mm)
1	Izas	47	19/10/2012 01:00	262.0	0.73	181.8
2	Caldo	130	12/12/2012 06:00	303.0	108.46	286.8
3		63	14/12/2019 10:00	326.9	139.22	289.2
4	Landro	48	24/01/2021 12:00	39.7	87.18	30.8
5		48	02/02/2021 00:00	33.6	49.66	20.6
6	Genil	96	20/10/2018 00:00	41.5	953.21	19.1
7		96	04/11/2020 00:00	45.7	354.28	4.1

Regardless of their origin, all these DTMs can include sinks that originate from an inadequate elevation precision and closed topographic depressions (O'Callaghan and Mark, 1984). The majority of depressions in DTMs are singularities caused by a failure of the source data to capture the topography's natural break lines, insufficient grid resolution, random errors that create flow blockages, and a surface model's inability to properly represent infrastructure such as culverts and bridges (Lindsay, 2016). Most hydrological applications of DTMs begin with sink removal to ensures continuous flow paths by flow enforcement techniques including filling and breaching methods (Martz and Garbrecht, 1998). This is a commonly used technique as not all hydrological models are able to work with DTMs that include depressions or even flat bottom. Also knowing that such depression-filling algorithms have been criticised in the academic literature for their greater impact on DTMs (Lindsay, 2016), the authors have avoided using such techniques in order to prevent disturbing the comparison between DTMs. Therefore, raw digital models have been used without applying any type of sink filling treatment.

3.2. Numerical model

Surface runoff was simulated using the numerical model Iber+ (García-Feal et al., 2018), which is a GPU-parallelized version of the Iber model (Bladé et al., 2014). Iber + is a 2D numerical model for simulating free surface flow and transport processes in shallow waters. Iber + allows calculating rainfall-runoff (hydrological) and inundation (hydraulic) processes in a coupled way, and it has been validated for rainfall-runoff modelling in multiple previous works (Cea et al., 2014, 2010; Cea and Bladé, 2015; Fraga et al., 2019, 2016; Sanz-Ramos et al., 2021). Its reliability and computational efficiency has even led Iber + to be recently incorporated in several flood early warning systems (Fernández-Nóvoa et al., 2020; Fraga et al., 2020; González-Cao et al., 2019).

The mass and momentum conservation equations solved by the model can be written as follows:

$$\frac{\partial h}{\partial t} + \frac{\partial q_x}{\partial x} + \frac{\partial q_y}{\partial y} = R - i \tag{1}$$

$$\frac{\partial q_x}{\partial t} + \frac{\partial}{\partial x}\left(\frac{q_x^2}{h} + g\frac{h^2}{2}\right) + \frac{\partial}{\partial y}\left(\frac{q_x q_y}{h}\right) = -gh\frac{\partial z_b}{\partial x} - g\frac{n^2}{h^{7/3}}|q|q_x \tag{2}$$

$$\frac{\partial q_y}{\partial t} + \frac{\partial}{\partial x}\left(\frac{q_x q_y}{h}\right) + \frac{\partial}{\partial y}\left(\frac{q_y^2}{h} + g\frac{h^2}{2}\right) = -gh\frac{\partial z_b}{\partial y} - g\frac{n^2}{h^{7/3}}|q|q_y \tag{3}$$

where h is the water depth, q_x, q_y and $|q|$ are the two components of the unit discharge and its modulus, z_b is the bed elevation, n is the Manning coefficient, g is the gravity acceleration, R is the rainfall intensity and i the infiltration rate. The source terms of precipitation and infiltration can vary in space and time and, since both terms are included independently in the hydrodynamic equations, infiltration can occur even in the absence of precipitation, as long as there is a positive water depth over a mesh element. Therefore, the possible effect of local topographic features on the infiltration rate is implicitly included in the equations. However, the numerical representation of this process will be dependent on the resolution of the DTM and computational mesh, since recent studies have shown that low-resolution models tend to poorly represent land surface features and therefore eliminate depressions and barriers that interrupt and retain flow, leading to a decrease in cumulative infiltration (Habtezion et al., 2016). The hydrodynamic equations are solved using an unstructured finite volume solver, which includes a specific numerical scheme for hydrological applications (Cea and Bladé,

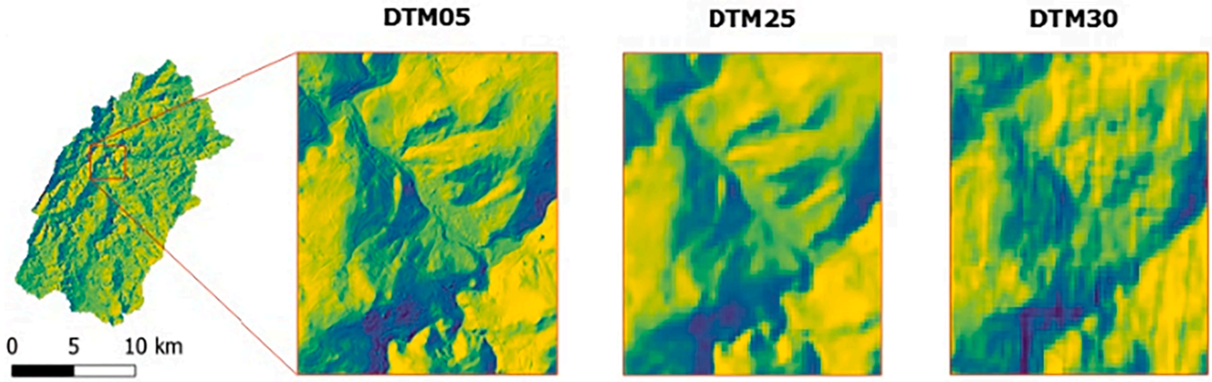

Fig. 2. Differences in the resolution of the DTMs used. As an example, it was taken the same river stretch of the Landro basin for DTM05 (left), DTM25 (centre) and DTM30 (right).

2015). This numerical scheme is first-order accurate in space and time.

The geometry of the four catchments was discretized using an unstructured and uniform mesh of triangular elements generated in GiD (Coll et al., 2018a, 2018b). GiD adapts the mesh size to the geometry of the model by approximating the element sizes to the value indicated by the modeler. The maximum relative error in this size approximation was set at 10%. The chosen element size is not constant in all catchments and is detailed in Section 3.3. Regarding the temporal accuracy of the models, the discretization used in this work is explicit in time, which implies that the computational time step is constrained by a stability condition (CFL condition). In addition, the dry-wet limit has been set equal to 0.1 mm in all simulations.

In Iber+, the DTM values are interpolated to the nodes of the computational mesh using a bilinear interpolation method. The elevation value at each mesh vertex is interpolated using the 4 DTM elevation values closest to the vertex being interpolated. Bottom friction is modelled in Iber + with the Manning's formula (Bladé et al., 2014). In this work the Manning coefficient was defined according to the land use map of the European project CORINE Land Cover 2018 (CLC2018) (European Union Copernicus Land Monitoring Service, 2018) and the recommendations of the Methodological Guide for the Development of the National Floodplain Mapping System (Ministerio de Medio Ambiente y Medio Rural y Marino, 2011), which proposes a Manning coefficient for each of the CORINE land uses. Infiltration was modelled following the SCS-CN methodology (Mockus, 1964). The single parameter of the model, the Curve Number (CN), was defined according to the rainfall registered the days prior to the start of the event, distinguishing between dry (CN I), normal (CN II) or wet (CN III) antecedent moisture conditions. Finally, it is worth mentioning that in all simulations a warm-up period of the model has been set until the base flow at the beginning of the event is reached.

Table 3 shows the Curve Number used for each event and the Manning coefficient values used for each basin. Due to the small size of the Izas basin, a constant CN value has been taken for the whole watershed. The Genil basin is characterised by low surface runoff coefficients (Table 2). While for the rest of the basins the surface runoff coefficient remains above 60%, in the events of the Genil river basin these values drop to 46% and 9%, respectively for events 6 and 7. Table 1 reveals that the Genil catchment is the basin with the lowest annual precipitation but with the highest maximum daily precipitation. The lowest value of CN is also found in this basin (Table 3). With respect to the rest of the watersheds, a coherence is observed between the Curve Number and the runoff coefficient for the analysed events.

Table 3
Curve Number and Manning coefficient values used in the numerical simulation of the models. For the Manning's coefficient, the range of values of the model is given. For the Curve Number, the range of variation and its mean value are given together with an indication of whether the antecedent conditions are dry (CN I), normal (CN II) or wet (CN III).

Event number	Watershed	Manning coefficient range ($m^{-1/3}s$)	Curve Number		
			Range	Mean	Antecedent moisture condition
1	Izas	[0.025 – 0.035]	73.84	73.84	CN II
2	Caldo	[0.025 – 0.07]	[51.90 – 86.40]	64.5	CN II
3			[71.30 – 93.60]	87.2	CN III
4	Landro	[0.035 – 0.062]	[71.31 – 93.59]	81.43	CN III
5			[71.31 – 93.59]	81.43	CN III
6	Genil	[0.025 – 0.1]	[51.42 – 98.07]	74.13	CN II
7			[30.77 – 95.52]	55.53	CN I

3.3. Spatial discretization

As previously mentioned, the spatial resolutions of the DTMs used in this study are 5, 25 and 30 m. To achieve a full exploitation of the DTM resolution, the cell size of the numerical mesh should be equal to, or lower than, the resolution of the DTM. However, the computational cost of using a very fine mesh in models that cover large areas can result in calculation times that are prohibitive for most practical applications, especially when using fully distributed hydrological models based on the 2D-SWE, which leads to the use of element sizes larger than the DTM resolution and results in a loss of topographical information. This can be partially improved by the use of non-uniform meshes, with smaller element sizes in the river network and larger sizes in the hillslopes (Costabile and Costanzo, 2021; Ferraro et al., 2020; Uber et al., 2021). This might improve the accuracy of the results without increasing too much the total number of elements. In order to simplify the analysis, in this work unstructured uniform meshes were considered.

Implementing a subgrid modelling approach can include some topographical information in the equations when the DTM resolution is much higher than the computational mesh resolution, in order to improve the results without affecting too much the computational time. Such kind of subgrid modelling approaches have been applied to the shallow water equations in previous studies (Platzek et al., 2016; Sanders and Schubert, 2019; Shen et al., 2015; Shustikova et al., 2019; Volp et al., 2013), but have not been used in the present model, since they are not implemented in most shallow water models.

The different size of the catchments analysed in this work (from 0.33 to 3750 km^2) made it impossible to use the same cell size in all the models due to computational cost limitations. In the Caldo and Landro basins, with an area of approximately 40 and 200 km^2, the element sizes were 10, 25 and 100 m. Smaller element sizes were not used since they would imply a very high computational cost, not affordable in practical applications. In the Izas basin (0.33 km^2) the element sizes used were 1, 2.5 and 10 m, in order to have some grids with a higher resolution than the finest DTMs. In the Genil basin (3750 km^2) it was not possible to reach the mesh resolutions used in the Caldo and Landro finest meshes, so the mesh sizes used were 25, 62.5 and 250 m.

Table 4 summarises the main characteristics of the computational grids used. A triangular unstructured uniform mesh was used in all cases. In the following, the mesh sizes will be denoted, according to its resolution, as fine, medium and coarse.

4. Results and discussion

4.1. Model validation

In order to analyse the degradation of the model output when working with a coarser mesh and a lower resolution DTM, the hydrographs computed with the fine mesh and the highest resolution DTM (DTM05) were taken as a reference value. Fig. 3 compares, for each event, the observed hydrograph with the simulated reference hydrograph. The visual comparison depicted in Fig. 3 and the values of MAE, NSE and relative error for hydrograph volume obtained for each case show a reasonably good agreement between numerical results and field data. MAE of each event has been normalised to the peak flow of the corresponding observed hydrograph to allow a comparison between the different events, obtaining an average MAE value of 7% of the peak flow. The values of the MAE/Qp and NSE indicators are satisfactory, however it can be observed that the adjustment of the hydrograph volumes in some events is not accurate, due to mismatches in the base flow of the numerical model.

4.2. Effect of the computational mesh and DTM resolutions

Fig. 4 shows the NSE coefficient obtained for each of the rainfall events and the overall performance of the different mesh sizes. The 3 DTMs have very different characteristics, so the results of each DTM have been represented in different subplots to help the further analysis. Regarding the differences between the results obtained for the DTM05 and the DTM25, the NSE values are practically analogous between both DTMs for all element sizes. Knowing that the DTM25 is a product created by the IGN from the DTM05, the results indicate that the vertical accuracy of the data is more relevant than the spatial horizontal resolution of the DTM itself. Furthermore, it can be seen that, at the same mesh resolution (fine), DTM25 provides comparable results to DTM05. This finding would not follow the trend identified by Habtezion et al. (2016), who noted that the DTM resolution threshold above which similar results are obtained is equal to 10 m. But in the comparison of the different DTMs, what is most remarkable is the poor results of the DTM30 in the larger catchments (events 4, 5, 6 and 7). Although its spatial horizontal resolution is not much higher than that of the DTM25, the NSE values in the Landro and Genil basins are low even for the finest meshes. Moving on to compare the results of the different mesh sizes, Fig. 4 shows remarkable good outcomes for the Izas basin, where, independently of the DTM used, the NSE values are always practically equal to 1. Regarding the results obtained in Caldo and Landro (where the element sizes are shared), the similarity of results between the fine mesh (10 m) and the medium mesh (25 m) is patent. This result is particularly interesting in the case of the DTM05, where the element size of the fine mesh could take advantage of the spatial resolution of the DTM. The differences obtained between the fine (10 m) and coarse (100 m) mesh, leaving aside the bad behaviour of the DTM30 in the case of the Landro, acquire a relative relevance in some cases such as event 4 for the DTM05 and DTM25, where the value of the NSE reaches 0.556 and 0.552, respectively. The differences in mesh element sizes lead to slightly different results in the Genil river basin. In the DTM05 and DTM25 (again, the DTM30 results do not seem to correspond to their lower resolution counterparts), the medium mesh (62.5 m) obtains results very close to those of the fine mesh (25 m), with values still above 0.716. However, a strong reduction of the NSE is perceived with the coarse mesh (250 m), particularly in event 7.

This degradation of the result as a function of element size is clearer in Fig. 5. This figure shows the NSE, normalized centred root-mean-square difference (E_n) (Taylor, 2001) and MAE results obtained for the different DTMs and in relation to the element size of each catchment. Regarding E_n, values below 0.5 are assumed to be good, as this limit has already been used as a reference in the analysis of streamflow series with this parameter (González-Cao et al., 2019). In the case of MAE, the result has been normalised to the peak flow of the reference hydrograph to facilitate the comparison between the different events. The correlation of the results has been estimated with Pearson's and Spearman's coefficients and their value is indicated for each of the subplots (r_P and r_S, respectively). Again, we find here a clear analogy between the NSE values obtained for the DTM05 and DTM25; and it is seen how this result holds with the E_n and MAE/Qp values too. Also, the DTM30 differs from the DTM05 and DTM25 especially for the Landro and Genil basins (the largest ones). A larger surface area in these catchment favours the appearance of outlier points with low accuracy which, together with the low runoff depth value of the events in Landro and Genil (relative to the Izas and Caldo events), intensifies the degradation of the outflow hydrograph. Regarding the results obtained for the mesh sizes, although the number of data is not high, a quasi-linear relationship is observed in the metrics corresponding to the DTM05 and DTM25. In particular, for both DTMs, the good results obtained from a threshold close to 25 m stand out, since all NSE values are above 0.913, E_n values are below 0.293 and MAE/Qp values are below 0.028. Apart from this, the results obtained with the DTM05 and DTM25 for the fine meshes are also remarkable.

As a representative example, Fig. 6 includes the hydrographs obtained for Event 5 (Landro river basin). In this figure it can be seen how, visually, the results obtained with the DTM05 and DTM25 for the fine and medium meshes are similar and very close to the reference hydrograph (finest mesh and DTM05). Another significant result is that DTM25 and especially the DTM30 (for fine and medium mesh) tend to underestimate the peak of the hydrograph. This pattern has been repeated in the rest of the events. These results are in line with what was highlighted by Habtezion et al. (2016), where it was observed that coarse resolution DTMs (>10 m) tend to overestimate ponded areas and therefore to reduce and delay the peak of the hydrograph. However, in view of the results obtained, where there is a large underestimation of the peak flow by the DTM30, at a different magnitude than the DTM25, it could be deduced that this trend is not only linked to the horizontal resolution of the DTM, but also to its vertical accuracy.

The outflow hydrograph can be affected by the water retention capacity of the DTM used. The effect that the study DTMs have on this accumulation of water on the model surface is shown in Fig. 7. Taking as

Table 4
Resolution of the computational meshes.

Watershed	Mesh size (m)	Number of elements (K)	Mesh Id.
Izas	10	7	Coarse
	2.5	116	Medium
	1	725	Fine
Caldo	100	9	Coarse
	25	127	Medium
	10	799	Fine
Landro	100	45	Coarse
	25	733	Medium
	10	4,587	Fine
Genil	250	119	Coarse
	62.5	1,933	Medium
	25	12,075	Fine

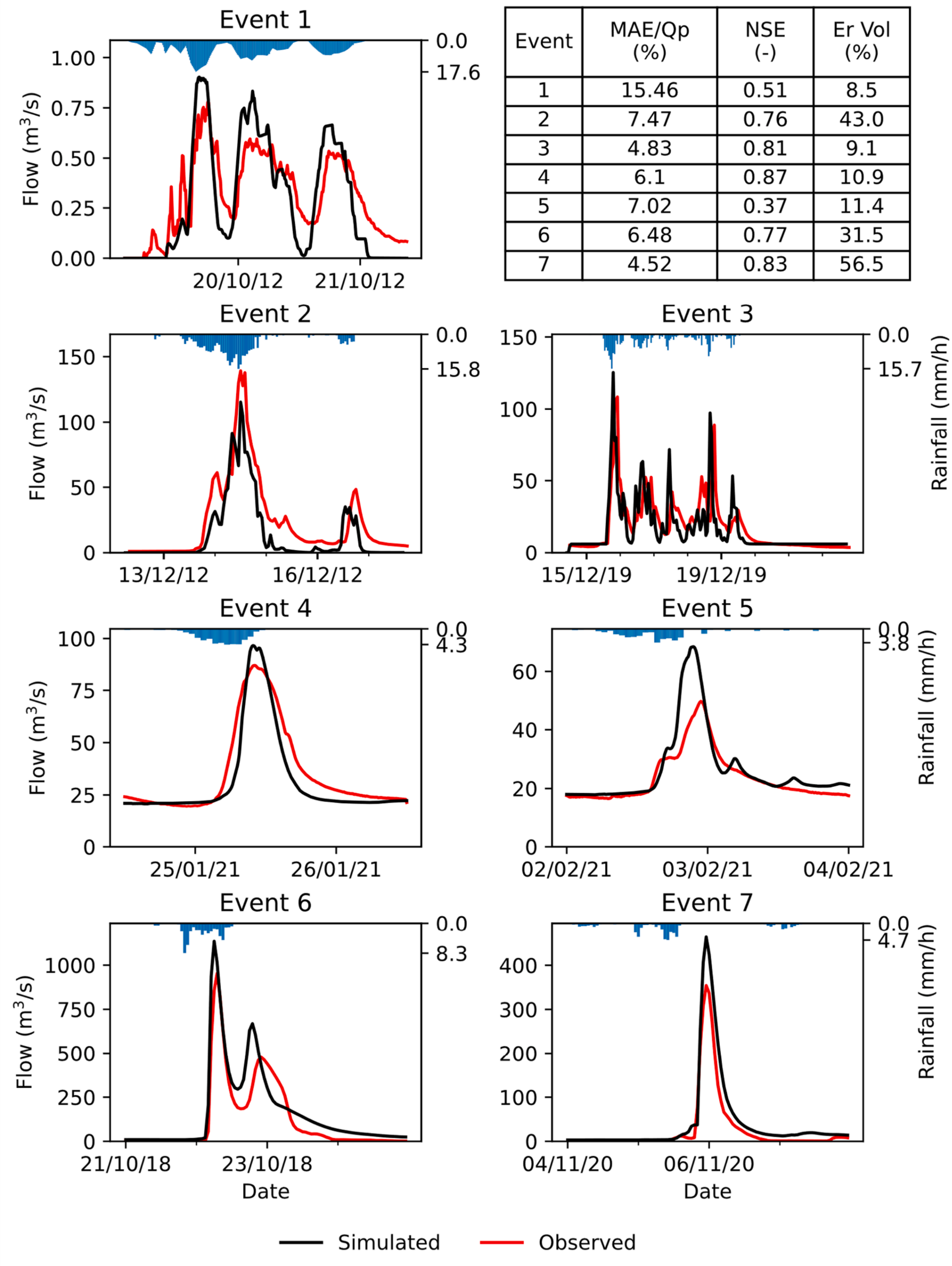

Event	MAE/Qp (%)	NSE (-)	Er Vol (%)
1	15.46	0.51	8.5
2	7.47	0.76	43.0
3	4.83	0.81	9.1
4	6.1	0.87	10.9
5	7.02	0.37	11.4
6	6.48	0.77	31.5
7	4.52	0.83	56.5

Fig. 3. Observed and simulated hydrographs for the 7 rainfall events. The simulated hydrographs were computed with the fine mesh and the 5 m resolution DTM (DTM05). In the upper right corner, it is summarized, for each event, MAE, NSE and the relative error of the volume of the hydrographs. The MAE values have been normalised to the corresponding peak flow observed in the event and are represented in percentage.

representative example the event 4 registered in the Landro river basin, Fig. 7 shows the spatial distribution of the maximum depths obtained for the 3 DTMs and the finest mesh. The model's runoff volume at each timestep has also been added. The results observed at Fig. 7 confirm the relevance of the DTM change in the model outcome. When the results obtained for the three DTMs are compared, it can be seen that, despite maintaining the same mesh resolution (fine) and despite having a DTM horizontal resolution close to the DTM25, DTM30 notably increase the surface storage capacity of the model. This increase in storage capacity is less relevant in the Izas and Caldo basins. In addition, this increase in storage capacity is also related to the increase in the size of the mesh elements. This effect influences the poor results of coarse meshes and, as Caviedes-Voullième et al. (2012) has already indicated, it is, in part, due to the poor topographic representation of the terrain. Since local minima

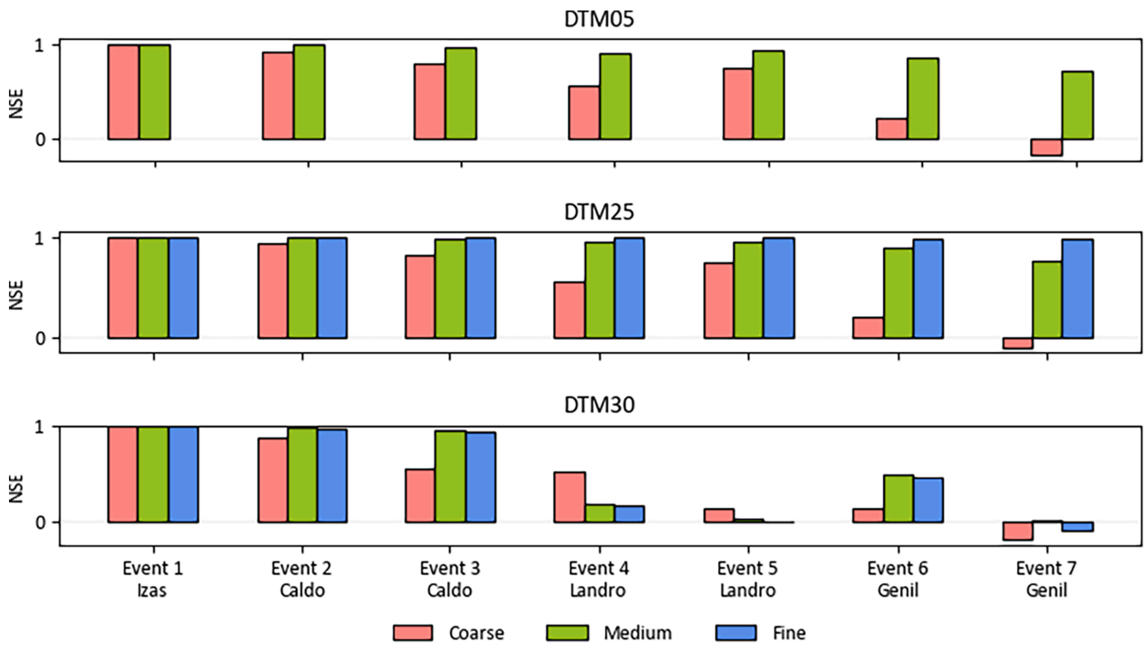

Fig. 4. NSE values obtained for each of the rainfall event simulations. Rainfall events have been ordered according to the size of the catchments from smallest (left) to largest (right). In red, green and blue, the results corresponding to the coarse, medium and fine mesh models, respectively. (For interpretation of the references to colour in this figure legend, the reader is referred to the web version of this article.)

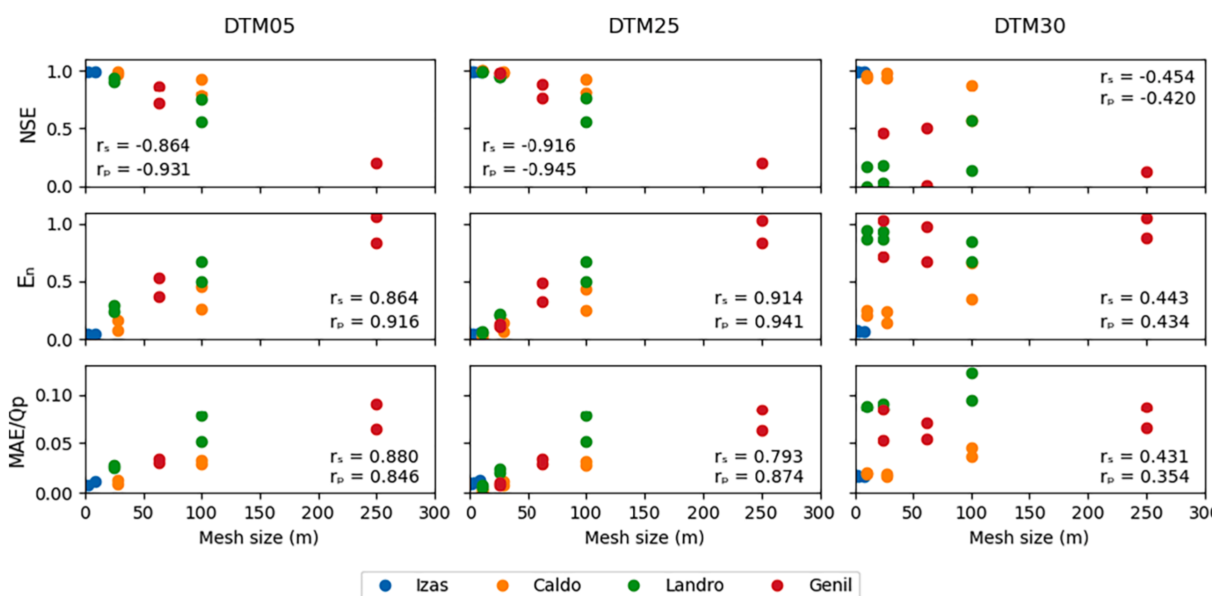

Fig. 5. Relationship between the values of NSE, normalized centred root-mean-square difference (E_n) and MAE/Qp, related to the mesh size for each of the catchments and for each of the DTMs. In blue, orange, green and red, the values corresponding to the Izas, Caldo, Landro and Genil catchments, respectively. In each subplot the values of Spearman's coefficient (r_S) and Pearson's coefficient (r_P) are indicated. (For interpretation of the references to colour in this figure legend, the reader is referred to the web version of this article.)

and maxima may be poorly represented with coarse meshes, which results in static, ponded water which cannot flow further. This effect is enhanced in events that have much lower peak flows (e.g., event 7 with lower peak flow than event 6).

For a better understanding of the differences obtained with the DTM30 regarding the DTM25 and DTM05 it is necessary to look at the origin of the DTMs themselves. The DTM05 and DTM25 are LiDAR-derived DTMs, however, DTM30 is created via InSAR (i.e., active sensor). Even though active sensors have its advantages over passive sensors (e.g., active sensors are considered to penetrate more the vegetation than an active sensor), it is a technique that cannot compete with the precision of LiDAR. In fact, in works such as Courty et al. (2019), where the accuracy of different open-access DTMs (including a SRTM product) in flood modelling is compared, the LiDAR-derived DTM values are taken as a reference for the evaluation criteria.

In order to analyse the effect of the different DTMs on the computational mesh, Fig. 8 shows the comparison between some cross-sections, belonging again to the Landro river basin, reproduced with the different calculation meshes used in the numerical simulations. In particular, as an example, three cross-sections have been considered. In line with previous statements, compared to the reference case (DTM05 and fine mesh), the performance of the DTM25 is remarkable, together

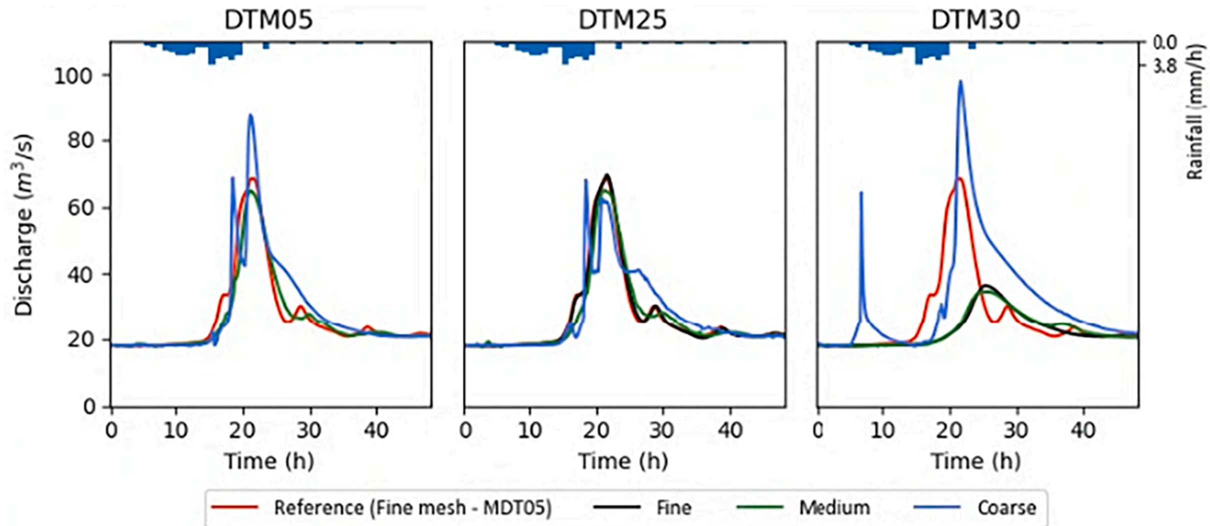

Fig. 6. Hydrographs obtained for event 5 (Landro river basin). Each of the figures respresents the results generated with the DTM05 (left), DTM25 (middle) and DTM30 (right). In red the hydrograph defined as reference. In black, green and blue, the results of the fine, medium and coarse mesh, respectively. (For interpretation of the references to colour in this figure legend, the reader is referred to the web version of this article.)

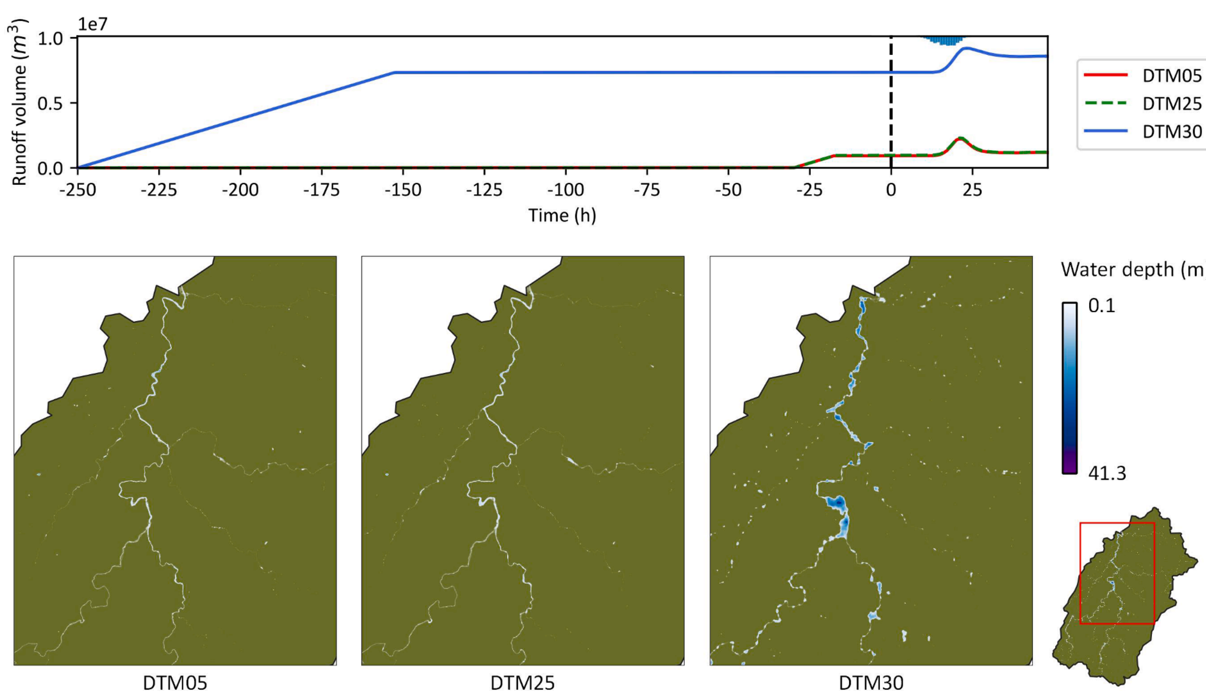

Fig. 7. Below, map of maximum depths obtained during the simulation of the event 4 (Landro river basin); on the left with DTM05, middle with DTM25 and on the right with DTM30. Above, model runoff volume for the different simulations (t = 0 h indicates the end of the model's warm-up period and the start of the event simulation). All the results in this figure were obtained with the fine mesh (10 m element size).

with the less accurate reproduction of DTM30. In the results obtained with the fine mesh, a MAE of less than 0.7 m has been obtained in the 3 sections related to DTM25 and, however, this value rises to more than 12 m in sections 1 and 2 corresponding to the DTM30. Furthermore, for DTM05 and DTM25, the results obtained with the medium mesh, reproduce reasonably well the profile obtained with the fine mesh (the maximum MAE is obtained in section 2 for DTM25 and is equal to 4.27 m). Nevertheless, with the coarse mesh, the obtained profiles are visibly far from a correct representation of the reference profile, greatly limiting the drainage capacity of the section. For example, the MAE resulted for DTM05 and coarse mesh in section 3 is equal to 10.62 m.

4.3. Runtime

The runtime increment of each simulation with respect to the runtime obtained with the DTM05 and the fine mesh is represented in Fig. 9. In general, the runtimes obtained with the DTM25 tend to be equal or slightly lower than those of the DTM05. This result is affected by the fact that the DTM25 is smoother than the DTM05, which results in somewhat higher depths or velocities being generated in some areas of the model in the latter case. Since the temporal discretization of the numerical model is subject to a Courant-Friedrichs-Lewy (CFL) stability constraint over the computational time step (Cea and Bladé, 2015), numerically, and under a constant element size, the increase in water velocity and depth is

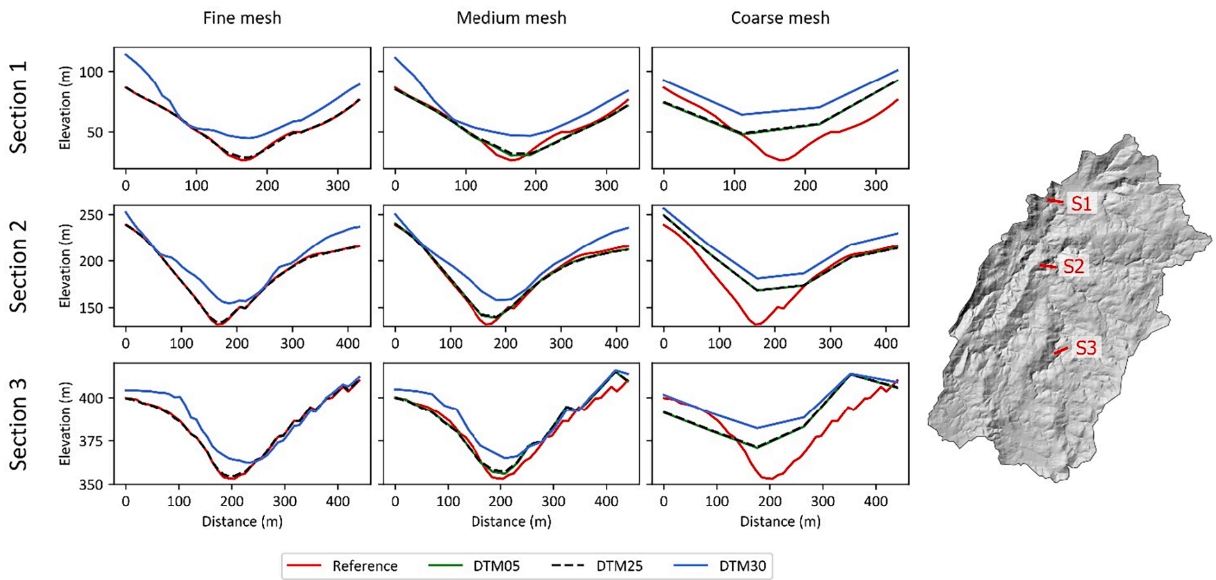

Fig. 8. Sections in the Landro river basin. Each row corresponds to a section and each column corresponds to a mesh size. Red line represents the reference result (DTM05 and fine mesh), green lines the results obtained with DTM05, black dotted line to the DTM25 and blue line to DTM30. (For interpretation of the references to colour in this figure legend, the reader is referred to the web version of this article.)

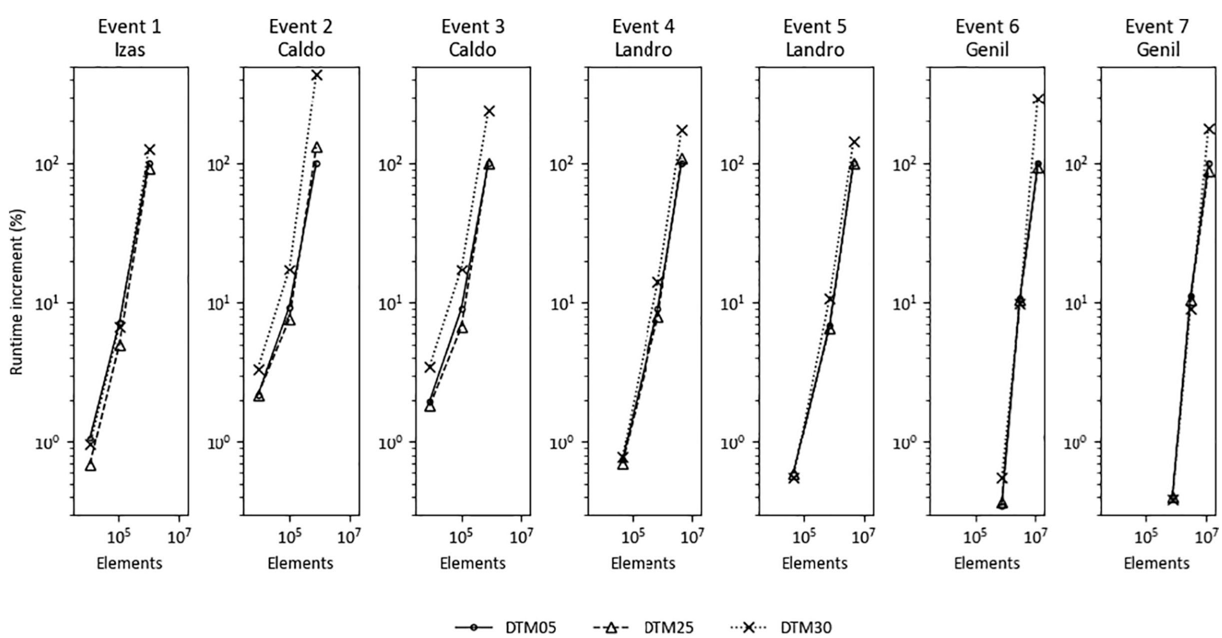

Fig. 9. Runtimes increments (%) obtained for each of the rainfall event simulations. Increments have been calculated with regard to runtime obtained for DTM05 and the fine mesh.

compensated by a reduction in the time step. This implies a smaller computational time step in the simulations performed with the DTM05, so its computation time is in general equal to or higher than that obtained in the DTM25 simulations. Something similar is also true for the DTM30. The runtimes obtained with this DTM tend to be always equal to or higher than the rest of the DTMs. DTM30 has a lower quality than the rest of DTMs, which causes significant water accumulations in the model that affect its runtime. In some cases, the difference in runtime increment of DTM30 is particularly relevant (e. g., event 6 and fine mesh). In these cases, the resolution of the mesh aggravates the imperfections of the DTM30 and has an effect on this increase in the runtime. The size of the mesh elements has a direct implication on the CFL condition. A larger element size leads to an increase in computational time step and therefore a decrease of the runtime. Overall, the use of the medium mesh (with elements 2.5 times larger than those of fine mesh) instead of the fine mesh results in a reduction of approximately 90% of the calculation time. The simulations carried out with the coarse mesh (with elements 10 times larger than those of fine mesh) further reduce the calculation time, reaching a reduction of more than 99% in Izas, Landro and Genil basins.

5. Conclusions

With the recent development of fully distributed hydrological models, and their application to large catchments, the spatial resolution of the mesh and model inputs becomes highly relevant. This study was intended to understand the effects that different DTM and mesh resolutions have on the simulation results both output hydrographs and runtimes. Thus, seven observed rainfall events corresponding to 4 basins have been selected to be modelled using the Iber + numerical model. Each of the events was simulated for 3 different mesh sizes and for 3 different DTMs, making a total of 63 simulations (9 per event). The hydrographs obtained for the higher resolution DTM and the finest mesh have been taken as a reference (synthetic observation).

The results obtained indicate that, under the same mesh resolution, the vertical accuracy of the DTM has a greater effect on the outflow hydrograph of the model than the horizontal resolution of the DTM. Despite a five-fold increase in spatial resolution, the results obtained with the 25 m DTM (DTM25) were very similar to those obtained with the 5 m DTM (DTM05). Results that have not been correctly reproduced by the 30 m DTM (DTM30). In addition, it has also been shown that mesh resolutions up to a threshold of 25 m, together with a LiDAR-based DTM with a horizontal resolution higher than 25 m, did provide comparable results with regard to the outlet hydrograph. The values obtained with a 25 m resolution mesh have achieved a minimum value of 0.913 in terms of NSE; maximum value of 0.293 of normalized centred root-mean-square difference (E_n) and 0.028 of MAE normalised to the peak flow, along with a 90% saving in runtime compared the result of a 2.5 times higher resolution mesh. In the application of fully distributed hydrological models based on the 2D shallow water equations, the use of global datasets should be limited only to those locations where LiDAR data are not available. In the case of using a lower resolution than the LiDAR-based DTM, the topography should be defined from a resampling of this product rather than from global datasets. These conclusions are consistent at least for fully distributed hydrological models based on the shallow water equations with a uniform unstructured computational mesh and only with regard to the outflow hydrograph of the basin. The possible degradation of other distributed hydrological outputs, such as depth and velocity maps, has not been analysed in this article but will be considered for further work.

CRediT authorship contribution statement

Gonzalo García-Alén: Conceptualization, Methodology, Writing – original draft. **Jose González-Cao:** Conceptualization, Methodology, Writing – original draft, Writing – review & editing. **Diego Fernández-Nóvoa:** Conceptualization, Methodology, Writing – original draft, Writing – review & editing. **Moncho Gómez-Gesteira:** Conceptualization, Methodology, Writing – review & editing, Supervision. **Luis Cea:** Conceptualization, Methodology, Writing – review & editing, Supervision. **Jerónimo Puertas:** Conceptualization, Methodology, Writing – review & editing, Supervision.

Declaration of Competing Interest

The authors declare that they have no known competing financial interests or personal relationships that could have appeared to influence the work reported in this paper.

Data availability

No data was used for the research described in the article.

Acknowledgments

The authors acknowledge the support of Augas de Galicia, the Galicia Meteorological Agency (Meteogalicia), the Automatic Hydrological Information System (SAIH) of the Miño-Sil River Basin Management Authority (CHMS), the Pyrenean Institute of Ecology (IPE) and the Automatic Hydrological Information System (SAIH) for the river Guadalquivir River Basin Management Authority (CHG) for providing the observed data for the assessment of the studied basins. DFN was supported by Xunta de Galicia through a post-doctoral grant (ED481B-2021-108). This work was partially financed by Xunta de Galicia, Consellería de Cultura, Educación e Universidade, under Project ED431C 2021/44 and ED431C 2018/56 from "Programa de Consolidación e Estructuración de Unidades de Investigación Competitivas". This work was partially funded by the European Regional Development Fund under the INTERREG-POCTEP project RISC_ML (Code: 0034_RISC_ML_6_E). Funding for open access charge: Universidade da Coruña/CISUG.

References

Alsdorf, D.E., Rodriguez, E., Lettenmaier, D.P., 2007. Measuring surface water from space. Rev. Geophys. 45 https://doi.org/10.1029/2006RG000197.

Alvera, B., García-Ruiz, J.M., 2000. Variability of Sediment Yield from a High Mountain Catchment, Central Spanish Pyrenees. Arctic. Antarct. Alp. Res. 32, 478–484. https://doi.org/10.1080/15230430.2000.12003392.

Barja, F.J.R., Lestegas, F.R., 1992. Os rios galegos: morfoloxía e rexime. Consello da Cultura Galega, Ponencia de Patrimonio Cultural.

Bellos, V., Papageorgaki, I., Kourtis, I., Vangelis, H., Kalogiros, I., Tsakiris, G., 2020. Reconstruction of a flash flood event using a 2D hydrodynamic model under spatial and temporal variability of storm. Nat. Hazards 101, 711–726. https://doi.org/10.1007/s11069-020-03891-3.

Berhanu, B., Melesse, A.M., Seleshi, Y., 2013. GIS-based hydrological zones and soil geo-database of Ethiopia. Catena 104, 21–31. https://doi.org/10.1016/j.catena.2012.12.007.

Bladé, E., Cea, L., Corestein, G., Escolano, E., Puertas, J., Vázquez-Cendón, E., Dolz, J., Coll, A., 2014. Iber: herramienta de simulación numérica del flujo en ríos. Rev. Int. Metod. Numer. para Calc. y Disen. en Ing. 30, 1–10. https://doi.org/10.1016/j.rimni.2012.07.004.

Bomers, A., Schielen, R.M.J., Hulscher, S.J.M.H., 2019. The influence of grid shape and grid size on hydraulic river modelling performance. Environ. Fluid Mech. 19, 1273–1294. https://doi.org/10.1007/s10652-019-09670-4.

Carrera-Hernandez, J.J., 2021. Not all DEMs are equal: An evaluation of six globally available 30 m resolution DEMs with geodetic benchmarks and LiDAR in Mexico. Remote Sens. Environ. 261 https://doi.org/10.1016/j.rse.2021.112474.

Caviedes-Voullième, D., García-Navarro, P., Murillo, J., 2012. Influence of mesh structure on 2D full shallow water equations and SCS Curve Number simulation of rainfall/runoff events. J. Hydrol. 448–449, 39–59. https://doi.org/10.1016/j.jhydrol.2012.04.006.

Cea, L., Bladé, E., 2015. A simple and efficient unstructured finite volume scheme for solving the shallow water equations in overland flow applications. Water Resour. Res. 51, 5464–5486. https://doi.org/10.1002/2014WR016547.

Cea, L., Garrido, M., Puertas, J., Jácome, A., Del Río, H., Suárez, J., 2010. Overland flow computations in urban and industrial catchments from direct precipitation data using a two-dimensional shallow water model. Water Sci. Technol. a. J. Int. Assoc. Water Pollut. Res. 62, 1998–2008. https://doi.org/10.2166/wst.2010.746.

Cea, L., Legout, C., Darboux, F., Esteves, M., Nord, G., 2014. Experimental validation of a 2D overland flow model using high resolution water depth and velocity data. J. Hydrol. 513, 142–153. https://doi.org/10.1016/j.jhydrol.2014.03.052.

Chen, Y., Li, J., Wang, H., Qin, J., Dong, L., 2017. Large-watershed flood forecasting with high-resolution distributed hydrological model. Hydrol. Earth Syst. Sci. 21, 735–749. https://doi.org/10.5194/hess-21-735-2017.

Chen, C., Yang, S., Li, Y., 2020. Accuracy Assessment and Correction of SRTM DEM Using ICESat/GLAS Data under Data Coregistration. Remote Sens. 12 (20), 3435.

Claessens, L., Heuvelink, G.B.M., Schoorl, J.M., Veldkamp, A., 2005. DEM resolution effects on shallow landslide hazard and soil redistribution modelling. Earth Surf. Process. Landforms J. Br. Geomorphol. Res. Gr. 30, 461–477. https://doi.org/10.1002/esp.1155.

Coll, A., Ribó, R., Pasenau, M., Escolano, E., Perez, J.S., Melendo, A., Monros, A., Gárate, J., 2018a. GiD v.14 Reference Manual.

Coll, A., Ribó, R., Pasenau, M., Escolano, E., Perez, J.S., Melendo, A., Monros, A., Gárate, J., 2018b. GiD v.14 User Manual.

Costabile, P., Costanzo, C., 2021. A 2D-SWEs framework for efficient catchment-scale simulations: Hydrodynamic scaling properties of river networks and implications for non-uniform grids generation. J. Hydrol. 599, 126306 https://doi.org/10.1016/j.jhydrol.2021.126306.

Costabile, P., Costanzo, C., Macchione, F., 2012. Comparative analysis of overland flow models using finite volume schemes. J. Hydroinformat. 14, 122–135. https://doi.org/10.2166/hydro.2011.077.

Costabile, P., Macchione, F., 2015. Enhancing river model set-up for 2-D dynamic flood modelling. Environ. Model. Softw. 67, 89–107. https://doi.org/10.1016/j.envsoft.2015.01.009.

Courty, L.G., Soriano-Monzalvo, J.C., Pedrozo-Acuña, A., 2019. Evaluation of open-access global digital elevation models (AW3D30, SRTM, and ASTER) for flood modelling purposes 12, 1–14. https://doi.org/10.1111/jfr3.12550.

Ministerio de Medio Ambiente y Medio Rural y Marino, 2011. Guía metodológica para el desarrollo del Sistema Nacional de Cartografía de Zonas Inundables.

Dietrich, W.E., Reiss, R., Hsu, M., Montgomery, D.R., 1995. A process-based model for colluvial soil depth and shallow landsliding using digital elevation data. Hydrol. Process. 9, 383–400. https://doi.org/10.1002/hyp.3360090311.

European Union Copernicus Land Monitoring Service, 2018. Corine Land Cover (CLC).

Farr, T.G., Rosen, P.A., Caro, E., Crippen, R., Duren, R., Hensley, S., Kobrick, M., Paller, M., Rodriguez, E., Roth, L., Seal, D., Shaffer, S., Shimada, J., Umland, J., Werner, M., Oskin, M., Burbank, D., Alsdorf, D., 2007. The shuttle radar topography mission. Rev. Geophys. 45 (2) https://doi.org/10.1029/2005RG000183.

Fernández-Nóvoa, D., García-Feal, O., González-Cao, J., de Gonzalo, C., Rodríguez-Suárez, J.A., Ruiz del Portal, C., Gómez-Gesteira, M., 2020. MIDAS: A New Integrated Flood Early Warning System for the Miño River. Water 12 (9), 2319.

Fernández-Pato, J., Caviedes-Voullième, D., García-Navarro, P., 2016. Rainfall/runoff simulation with 2D full shallow water equations: Sensitivity analysis and calibration of infiltration parameters. J. Hydrol. 536, 496–513. https://doi.org/10.1016/j.jhydrol.2016.03.021.

Fernández-Pato, J., Morales-Hernández, M., García-Navarro, P., 2018. Implicit finite volume simulation of 2D shallow water flows in flexible meshes. Comput. Methods Appl. Mech. Eng. 328, 1–25. https://doi.org/10.1016/j.cma.2017.08.050.

Ferraro, D., Costabile, P., Costanzo, C., Petaccia, G., Macchione, F., 2020. A spectral analysis approach for the a priori generation of computational grids in the 2-D hydrodynamic-based runoff simulations at a basin scale. J. Hydrol. 582, 124508. https://doi.org/10.1016/j.jhydrol.2019.124508.

Fraga, I., Cea, L., Puertas, J., Suárez, J., Jiménez, V., Jácome, A., 2016. Global sensitivity and GLUE-based uncertainty analysis of a 2D–1D dual urban drainage model. J. Hydrol. Eng. 21, 1–11. https://doi.org/10.1061/(ASCE)HE.1943-5584.0001335.

Fraga, I., Cea, L., Puertas, J., 2019. Effect of rainfall uncertainty on the performance of physically based rainfall–runoff models. Hydrol. Process. 33 (1), 160–173.

Fraga, I., Cea, L., Puertas, J., 2020. MERLIN: a flood hazard forecasting system for coastal river reaches. Nat. Hazards 100, 1171–1193. https://doi.org/10.1007/s11069-020-03855-7.

García-Alén, G., García-Fonte, O., Cea, L., Pena, L., Puertas, J., 2021. Modelling Weirs in Two-Dimensional Shallow Water Models. Water. https://doi.org/10.3390/w13162152.

García-Feal, O., González-Cao, J., Gómez-Gesteira, M., Cea, L., Domínguez, J.M., Formella, A., 2018. An accelerated tool for flood modelling based on Iber. Water (Switzerland) 10, 1–23. https://doi.org/10.3390/w10101459.

Gómez Gutiérrez, A., Conoscenti, C., Angileri, S., Rotigliano, E., Schnabel, S., 2015. Using topographical attributes to model the spatial distribution of gullying from two Mediterranean basins: advantages and limitations. Nat. Hazards 10, 291–314. https://doi.org/10.1007/s11069-015-1703-0.

González-Cao, J., García-Feal, O., Fernández-Nóvoa, D., Domínguez-Alonso, J.M., Gómez-Gesteira, M., 2019. Towards an automatic early warning system of flood hazards based on precipitation forecast: the case of the Miño River (NW Spain). Nat. Hazards Earth Syst. Sci. 19, 2583–2595. https://doi.org/10.5194/nhess-19-2583-2019.

Habtezion, N., Tahmasebi Nasab, M., Chu, X., 2016. How does DEM resolution affect microtopographic characteristics, hydrologic connectivity, and modelling of hydrologic processes? Hydrol. Process. 30, 4870–4892. https://doi.org/10.1002/hyp.10967.

Hancock, G.R., Martinez, C., Evans, K.G., Moliere, D.R., 2006. A comparison of SRTM and high-resolution digital elevation models and their use in catchment geomorphology and hydrology: Australian examples. Earth Surf. Process. Landforms 31, 1394–1412. https://doi.org/10.1002/esp.1335.

Hoch, J.M., van Beek, R., Winsemius, H.C., Bierkens, M.F.P., 2018. Benchmarking flexible meshes and regular grids for large-scale fluvial inundation modelling. Adv. Water Resour. 121, 350–360. https://doi.org/10.1016/j.advwatres.2018.09.003.

Hou, J., Wang, R., Liang, Q., Li, Z., Huang, M.S., Hinkelmann, R., 2018a. Efficient surface water flow simulation on static Cartesian grid with local refinement according to key topographic features. Comput. Fluids 176, 117–134. https://doi.org/10.1016/j.compfluid.2018.03.024.

Hou, J., Wang, T., Li, P., Li, Z., Zhang, X., Zhao, J., Hinkelmann, R., 2018b. An implicit friction source term treatment for overland flow simulation using shallow water flow model. J. Hydrol. 564, 357–366. https://doi.org/10.1016/j.jhydrol.2018.07.027.

Hu, R., Fang, F., Salinas, P., Pain, C.C., Domingo, N.D.S., Mark, O., 2019. Numerical simulation of floods from multiple sources using an adaptive anisotropic unstructured mesh method. Adv. Water Resour. 123, 173–188. https://doi.org/10.1016/j.advwatres.2018.11.011.

IGN-CNIG, 2021. Instituto Geográfico Nacional [WWW Document]. Cent, Descargas del CNIG http://centrodedescargas.cnig.es/CentroDescargas/index.jsp.

Kang, H., Sridhar, V., 2017. Combined statistical and spatially distributed hydrological model for evaluating future drought indices in Virginia. J. Hydrol. Reg. Stud. 12, 253–272. https://doi.org/10.1016/j.ejrh.2017.06.003.

Kellndorfer, J., Walker, W., Pierce, L., Dobson, C., Fites, J.A., Hunsaker, C., Vona, J., Clutter, M., 2004. Vegetation height estimation from Shuttle Radar Topography Mission and National Elevation Datasets. Remote Sens. Environ. 93, 339–358. https://doi.org/10.1016/j.rse.2004.07.017.

Kienzle, S., 2004. The effect of DEM raster resolution on first order, second order and compound terrain derivatives. Trans. GIS 8, 83–111. https://doi.org/10.1111/j.1467-9671.2004.00169.x.

Lacasta, A., Morales-Hernández, M., Murillo, J., García-Navarro, P., 2015. GPU implementation of the 2D shallow water equations for the simulation of rainfall/runoff events. Environ. Earth Sci. 74, 7295–7305. https://doi.org/10.1007/s12665-015-4215-z.

Laiolo, P., Gabellani, S., Campo, L., Silvestro, F., Delogu, F., Rudari, R., Pulvirenti, L., Boni, G., Fascetti, F., Pierdicca, N., Crapolicchio, R., Hasenauer, S., Puca, S., 2016. Impact of different satellite soil moisture products on the predictions of a continuous distributed hydrological model. Int. J. Appl. Earth Obs. Geoinf. 48, 131–145. https://doi.org/10.1016/j.jag.2015.06.002.

Lana-Renault, N., Nadal-Romero, E., Serrano-Muela, M.P., Alvera, B., Sánchez-Navarrete, P., Sanjuan, Y., García-Ruiz, J.M., 2014. Comparative analysis of the response of various land covers to an exceptional rainfall event in the central Spanish Pyrenees, October 2012. Earth Surf. Process. Landforms 39, 581–592. https://doi.org/10.1002/esp.3465.

Lehner, B., Döll, P., 2004. Development and validation of a global database of lakes, reservoirs and wetlands. J. Hydrol. 296, 1–22. https://doi.org/10.1016/j.jhydrol.2004.03.028.

Liang, D., Özgen, I., Hinkelmann, R., Xiao, Y., Chen, J.M., 2015. Shallow water simulation of overland flows in idealised catchments. Environ. Earth Sci. 74, 7307–7318. https://doi.org/10.1007/s12665-015-4744-5.

Lindsay, J.B., 2016. Efficient hybrid breaching-filling sink removal methods for flow path enforcement in digital elevation models. Hydrol. Process. 30, 846–857. https://doi.org/10.1002/hyp.10648.

López-Moreno, J.I., Pomeroy, J.W., Revuelto, J., Vicente-Serrano, S.M., 2013. Response of snow processes to climate change: spatial variability in a small basin in the Spanish Pyrenees. Hydrol. Process. 27, 2637–2650. https://doi.org/10.1002/hyp.9408.

Luis, C., Gabriela, V., Gonzalo, G.-A., Jerónimo, P., Luis, P., 2022. Hydraulic Modeling of Bridges in Two-Dimensional Shallow Water Models. J. Hydraul. Eng. 148, 6022006. https://doi.org/10.1061/(ASCE)HY.1943-7900.0001992.

Macchione, F., Lombardo, M., 2021. Roughness-Based Method for Simulating Hydraulic Consequences of Both Woody Debris Clogging and Breakage at Bridges in Basin-Scale Flood Modeling. Water Resour. Res. 57, e2021WR030485. 10.1029/2021WR030485.

Marsh, C.B., Spiteri, R.J., Pomeroy, J.W., Wheater, H.S., 2018. Multi-objective unstructured triangular mesh generation for use in hydrological and land surface models. Comput. Geosci. 119, 49–67. https://doi.org/10.1016/j.cageo.2018.06.009.

Martínez, L., Luis, J., Pascual, R., 2004. La calidad en la información geográfica de productos vectoriales del IGN, in: VIII Congreso Nacional de Topografía y Cartografía. Madrid.

Martz, L.W., Garbrecht, J., 1998. The treatment of flat areas and depressions in automated drainage analysis of raster digital elevation models. Hydrol. Process. 12, 843–855. https://doi.org/10.1002/(SICI)1099-1085(199805)12:6<843::AID-HYP658>3.0.CO;2-R.

Meléndez-Asensio, M., del Pozo-Tejado, J., 2019. Nueva delimitación de las masas de agua subterránea de la demarcación hidrográfica del Miño-Sil y su caracterización hidrogeológica. Ministerio de Ciencia, Innovación y Universidades del Gobierno de España, Ministerio para la Transición Ecológica.

Mockus, V., 1964. National engineering handbook. US Soil Conserv. Serv, Washington, DC, USA, p. 4.

Muhadi, N.A., Abdullah, A.F., Bejo, S.K., Mahadi, M.R., Mijic, A., 2020. The Use of LiDAR-Derived DEM in Flood Applications: A Review. Remote Sens. https://doi.org/10.3390/rs12142308.

Mujumdar, P.P., Nagesh Kumar, D., 2012. Floods in a changing climate: Hydrologic modeling, Floods in a Changing Climate: Hydrologic Modeling. Cambridge University Press. 10.1017/CBO9781139088428.

Mukherjee, S., Joshi, P.K., Mukherjee, S., Ghosh, A., Garg, R.D., Mukhopadhyay, A., 2012. Evaluation of vertical accuracy of open source Digital Elevation Model (DEM). Int. J. Appl. Earth Obs. Geoinf. 21, 205–217. https://doi.org/10.1016/j.jag.2012.09.004.

Mukul, M., Srivastava, V., Mukul, M., 2015. Analysis of the accuracy of Shuttle Radar Topography Mission (SRTM) height models using International Global Navigation Satellite System Service (IGS) Network. J. Earth Syst. Sci. 124, 1343–1357. https://doi.org/10.1007/s12040-015-0597-2.

Mukul, M., Srivastava, V., Jade, S., Mukul, M., 2017. Uncertainties in the Shuttle Radar Topography Mission (SRTM) Heights: Insights from the Indian Himalaya and Peninsula. Sci. Rep. 7, 41672. https://doi.org/10.1038/srep41672.

NASA JPL, 2013. NASA Shuttle Radar Topography Mission Global 1 arc second [WWW Document]. 10.5067/MEASURES/SRTM/SRTMGL1.003.

Ni, Y., Cao, Z., Liu, Q., Liu, Q., 2020. A 2D hydrodynamic model for shallow water flows with significant infiltration losses. Hydrol. Process. 34, 2263–2280. https://doi.org/10.1002/hyp.13722.

Ninyerola, M., Pons, X., Roure, J.M., 2005. Atlas climático digital de la Península Ibérica Metodología y aplicaciones en bioclimatología y geobotánica Información. Universitat Autònoma de Barcelona Departament de Biologia Animal, Biologia Vegetal i Ecologia (Unitat de Botànica) Departament de Geografia.

O'Callaghan, J.F., Mark, D.M., 1984. The extraction of drainage networks from digital elevation data. Comput. Vision Graph. Image Process. 28, 323–344. https://doi.org/10.1016/S0734-189X(84)80011-0.

Paulin, G.L., Bursik, M., Lugo-Hubp, J., Orozco, J.J.Z., 2010. Effect of pixel size on cartographic representation of shallow and deep-seated landslide, and its collateral effects on the forecasting of landslides by SINMAP and Multiple Logistic Regression landslide models. Phys. Chem. Earth, Parts A/B/C 35, 137–148. https://doi.org/10.1016/j.pce.2010.04.008.

Perumal, M., Price, R.K., 2017. Reservoir and channel routing Chapter 52, in: Singh V. P. (Ed) Handbook of Applied Hydrology. pp. 52-1-52–16.

Petaccia, G., Leporati, F., Torti, E., 2016. OpenMP and CUDA simulations of Sella Zerbino Dam break on unstructured grids. Comput. Geosci. 20, 1123–1132. https://doi.org/10.1007/s10596-016-9580-5.

Pham, H. V., Tsai, F.T., 2017. Groundwater modeling. Chapter 58, in: Singh V. P. (Ed) Handbook of Applied Hydrology. pp. 48-1-48–8.

Platzek, F.W., Stelling, G.S., Jankowski, J.A., Patzwahl, R., Pietrzak, J.D., 2016. An efficient semi-implicit subgrid method for free-surface flows on hierarchical grids. Int. J. Numer. Methods Fluids 80, 715–741.

PNOA, 2015. Tecnología LiDAR: Especificaciones técnicas [WWW Document]. accessed 11.2.21. https://pnoa.ign.es/especificaciones-lidar.

Quinn, P., Beven, K., Chevallier, P., Planchon, O., 1991. The prediction of hillslope flow paths for distributed hydrological modelling using digital terrain models. Hydrol. Process. 5, 59–79. https://doi.org/10.1002/hyp.3360050106.

Refsgaard, J.C., Storm, B., 1990. Construction, Calibration and Validation of Hydrological Models, in Distributed Hydrological Modelling. Springer, Dordrecht, The Netherlands. https://doi.org/10.1007/978-94-009-0257-2_3.

Revuelto, J., Azorin-Molina, C., Alonso-González, E., Sanmiguel-Vallelado, A., Navarro-Serrano, F., Rico, I., López-Moreno, J.I., 2017. Observations of snowpack distribution and meteorological variables at the Izas Experimental Catchment (Spanish Pyrenees) from 2011 to 2017 [Data set]. 10.5281/zenodo.848277.

Sanders, B.F., Schubert, J.E., 2019. PRIMo: Parallel raster inundation model. Adv. Water Resour. 126, 79–95. https://doi.org/10.1016/j.advwatres.2019.02.007.

Santillan, J.R., Makinano-Santillan, M., 2016. Vertical Accuracy Assessment of 30-M Resolution Alos, Aster, and Srtm Global Dems Over Northeastern Mindanao, Philippines. Int. Arch. Photogramm. Remote Sens. Spat. Inf. Sci. 41 https://doi.org/10.5194/isprs-archives-XLI-B4-149-2016.

Sanz-Ramos, M., Bladé, E., González-Escalona, F., Olivares, G., Aragón-Hernández, J.L., 2021. Interpreting the Manning Roughness Coefficient in Overland Flow Simulations with Coupled Hydrological-Hydraulic Distributed Models. Water. https://doi.org/10.3390/w13233433.

Savant, G., Trahan, C.J., Pettey, L., McAlpin, T.O., Bell, G.L., McKnight, C.J., 2019. Urban and overland flow modeling with dynamic adaptive mesh and implicit diffusive wave equation solver. J. Hydrol. 573, 13–30. https://doi.org/10.1016/j.jhydrol.2019.03.061.

Schaake, J.C., Koren, V.I., Duan, Q.Y., Mitchell, K., Chen, F., 1996. Simple water balance model for estimating runoff at different spatial and temporal scales. J. Geophys. Res. Atmos. 101, 7461–7475. https://doi.org/10.1029/95JD02892.

Shen, D., Wang, J., Cheng, X., Rui, Y., Ye, S., 2015. Integration of 2-D hydraulic model and high-resolution lidar-derived DEM for floodplain flow modeling. Hydrol. Earth Syst. Sci. 19, 3605–3616.

Shustikova, I., Domeneghetti, A., Neal, J.C., Bates, P., Castellarin, A., 2019. Comparing 2D capabilities of HEC-RAS and LISFLOOD-FP on complex topography. Hydrol. Sci. J. 64, 1769–1782.

Simons, F., Busse, T., Hou, J., Özgen, I., Hinkelmann, R., 2014. A model for overland flow and associated processes within the Hydroinformatics Modelling System. J. Hydroinformat. 16, 375–391. https://doi.org/10.2166/hydro.2013.173.

Singh, V.P., 2018. Hydrologic modeling: progress and future directions. Geosci. Lett. 5 https://doi.org/10.1186/s40562-018-0113-z.

Sreedevi, P.D., Owais, S., Khan, H.H., Ahmed, S., 2009. Morphometric Analysis of a Watershed of South India Using SRTM Data and GIS. J. Geol. Soc. INDIA 73, 543–552. https://doi.org/10.1007/s12594-009-0038-4.

Szabó, G., Singh, S.K., Szabó, S., 2015. Slope angle and aspect as influencing factors on the accuracy of the SRTM and the ASTER GDEM databases. Phys. Chem. Earth, Parts A/B/C 83, 137–145. https://doi.org/10.1016/j.pce.2015.06.003.

Tarolli, P., Tarboton, D.G., 2006. A new method for determination of most likely landslide initiation points and the evaluation of digital terrain model scale in terrain stability mapping. Hydrol. Earth Syst. Sci. 10, 663–677. https://doi.org/10.5194/hess-10-663-2006.

Taylor, K.E., 2001. Summarizing multiple aspects of model performance in a single diagram. J. Geophys. Res. Atmos. 106, 7183–7192. https://doi.org/10.1029/2000JD900719.

Tsangaratos, P., Ilia, I., Hong, H., Chen, W., Xu, C., 2017. Applying Information Theory and GIS-based quantitative methods to produce landslide susceptibility maps in Nancheng County, China. Landslides 14, 1091–1111. https://doi.org/10.1007/s10346-016-0769-4.

Uber, M., Nord, G., Legout, C., Cea, L., 2021. How do modeling choices and erosion zone locations impact the representation of connectivity and the dynamics of suspended sediments in a multi-source soil erosion model? Earth Surf. Dynam. 9, 123–144. https://doi.org/10.5194/esurf-9-123-2021.

Uuemaa, E., Ahi, S., Montibeller, B., Muru, M., Kmoch, A., 2020. Vertical Accuracy of Freely Available Global Digital Elevation Models (ASTER, AW3D30, MERIT, TanDEM-X, SRTM, and NASADEM). Remote Sens. https://doi.org/10.3390/rs12213482.

Vacondio, R., Dal Palù, A., Mignosa, P., 2014. GPU-enhanced finite volume shallow water solver for fast flood simulations. Environ. Model. Softw. 57, 60–75. https://doi.org/10.1016/j.envsoft.2014.02.003.

Vaze, J., Teng, J., Spencer, G., 2010. Impact of DEM accuracy and resolution on topographic indices. Environ. Model. Softw. 25, 1086–1098. https://doi.org/10.1016/j.envsoft.2010.03.014.

Volp, N.D., Van Prooijen, B.C., Stelling, G.S., 2013. A finite volume approach for shallow water flow accounting for high-resolution bathymetry and roughness data. Water Resour. Res. 49, 4126–4135.

Werner, M., 2001. Shuttle radar topography mission (SRTM) mission overview. Frequenz 55, 75–79. https://doi.org/10.1515/FREQ.2001.55.3-4.75.

Wilson, J.P., Repetto, P.L., Snyder, R.D., 2000. Effect of data source, grid resolution, and flow routing method on computed topographic attributes. Terrain Analysis: Principles Applications 133–161.

Xia, X., Liang, Q., Ming, X., 2019. A full-scale fluvial flood modelling framework based on a high-performance integrated hydrodynamic modelling system (HiPIMS). Adv. Water Resour. 132, 103392. https://doi.org/10.1016/j.advwatres.2019.103392.

Zhao, S., Qi, D., Li, R., Cheng, W., Zhou, C., 2021. Performance comparison among typical open global DEM datasets in the Fenhe River Basin of China. Eur. J. Remote Sens. 54, 145–157. https://doi.org/10.1080/22797254.2021.1891577.